Available online at www.sciencedirect.com

SCIENCE DIRECT®

Journal of Computational Physics 200 (2004) 299–324

JOURNAL OF COMPUTATIONAL PHYSICS

www.elsevier.com/locate/jcp

Numerical simulations of inviscid capillary pinchoff

Monika Nitsche [a,*], Paul H. Steen [b]

[a] *Department of Mathematics and Statistics, University of New Mexico, New Mexico, USA*
[b] *Department of Chemical and Biomolecular Engineering, Cornell University, USA*

Received 25 October 2003; received in revised form 9 March 2004; accepted 5 April 2004

Abstract

Inviscid capillary pinchoff is studied numerically, for an axisymmetric model problem in which a bubble pinches at two points on the symmetry plane, breaking into two symmetric end-bubbles and a satellite bubble in between. Results are presented for a range of density jumps across the bubble. The numerical method uses a formulation in terms of arclength and tangent angle, and incorporates a new procedure to redistribute the computational points dynamically, in order to maintain resolution in regions of high curvature. The results are compared with alternative computations by Lepinnen and Lister [Phys. Fluids 15 (2003) 568], where available. New results include details about the cone–crater structure near pinchoff, and the dependence of satellite bubble volume and pinchoff time on the density ratio.

Keywords: Surface tension; Axisymmetric vortex sheet; Inviscid capillary pinchoff; Interfacial flows

---

1. Introduction

This work presents numerical simulations of surface tension driven collapse and pinchoff of a soap film with subsequent satellite bubble formation. An experiment performed by Robinson and Steen [39] illustrates such a pinchoff process. In the experiment, an axisymmetric soap film is stretched between two circular coaxial rings to which the film is pinned. If the separation distance between the rings is below a critical value, the sleeve-like film is at equilibrium and takes on a catenoid shape. At a critical separation distance, the catenoidal equilibrium shape becomes neutrally stable. By slowly increasing the separation distance, the film suddenly becomes unstable and collapses. It pinches at two points on the symmetry axis, leading to disconnection into three pieces: two endpieces that relax to planar disks spanning the end rings, and a satellite bubble in between which eventually relaxes to a sphere. Understanding the pinchoff and satellite bubble formation process is relevant to many engineering processes. For example, control of liquid droplet size is crucial to many atomization processes (fuel combustion and fertilizer application) and to

---

[*] Corresponding author.
E-mail addresses: nitsche@math.unm.edu (M. Nitsche), phs7@cornell.edu (P.H. Steen).

0021-9991/$ - see front matter
doi:10.1016/j.jcp.2004.04.005

drop-on-demand technologies (inkjet printing and DNA arraying) [4,12]. Furthermore, features of the topological change that occurs at pinchoff are shared by a range of forming processes [44]. While our ultimate goal is to accurately simulate the described experiment to better understand pinchoff, this paper concerns an inviscid model problem.

Pinchoff is driven by surface tension, which can be resisted by either inertia or viscosity of the underlying fluid. In both cases, arguments on dimensional grounds predict that the pinchoff is self-similar, but with different scaling laws for the length scales near pinchoff. In practice, inviscid flow is an appropriate model when surface tension is resisted primarily by fluid inertia. This can occur over decades of length scales, reaching down to below the micron scale for water pinching in air, for example [4]. Thus, inviscid pinchoff is of practical importance on its own. Observation is consistent with theoretical predictions of self-similarity [39].

There is a large literature devoted to the study of viscous and inviscid pinchoff. We now mention a few of the numerous studies. Modern interest can be traced to the work of Keller and Miksis [24], who studied how surface tension drives inviscid flow, starting from a wedge-shaped geometry, and found a global self-similar solution for this 2D initial condition. Axisymmetric inviscid flows were then analyzed using a slenderness assumption that leads to a one-dimensional model [23,25,34,46]. For an axisymmetric surface of revolution $\mathbf{x}(s) = (r(s), z(s))$, where s is arclength, r is the radial coordinate and z is the symmetry axis, pinchoff is driven by the principal curvatures

$$\kappa_z = r_s z_{ss} - z_s r_{ss}, \quad \kappa_r = z_s/r, \tag{1.1}$$

through the Laplace–Young law (see Fig. 1). When viscosity is present, κ_r goes to infinity first and there is self-consistency of the one-dimensional models [16,17,41]. However, the axisymmetric slenderness assumption breaks down in inviscid flow, since κ_z grows large before κ_r [35]. In this case, overturning occurs before pinchoff. Like the 2D-wedge geometry, self-similarity is expected but now both principal curvatures are involved and a global self-similar solution is not possible. Experiments [36] and computations [28,43] are consistent with overturning before pinchoff and later computations clearly capture the overturning and subsequent self-similarity [13,15,27]. Analysis of the inviscid axisymmetric case remains of interest, both for applications and to better understand the mathematical nature of the finite-time singularity represented by pinchoff.

In this paper, we investigate inviscid axisymmetric pinchoff numerically. The soap film is modelled by a surface tension driven vortex sheet: an infinitely thin surface separating regions of potential fluid, across which the tangential velocity is discontinuous. Guided by Nie's [30] work, we consider a model problem of an initially spherical bubble that, at a critical time, pinches off at two points on the axis, disconnecting into

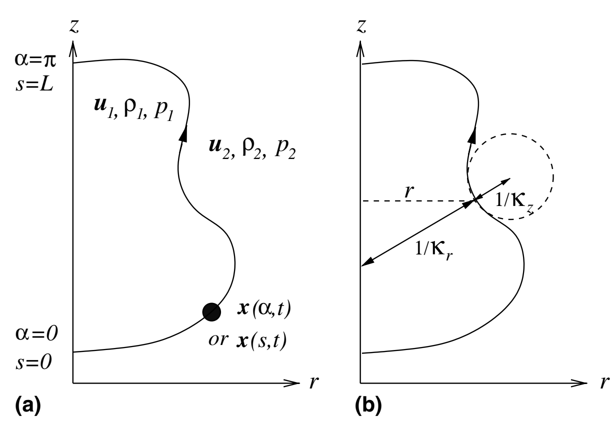

Fig. 1. Sketch illustrating: (a) axisymmetric vortex sheet, (b) principal curvatures κ_r, κ_z.

two symmetric end-bubbles and a satellite bubble in between, therefore resembling the pinchoff observed experimentally. In the model, the densities inside and outside the bubble may differ and a range of possible density jumps is considered. In the experiment, such a situation could be achieved by closing the endrings. The present objectives are to develop an accurate and stable numerical method, and to use the results to gain insight into the dynamics near pinchoff and its dependence on the density jump.

In the vortex sheet model, pinchoff corresponds to a finite-time singularity of the governing partial differential equations in which the curvatures grow unbounded. Resolving the singularity requires resolving many orders of length and timescales. This has been particularly difficult for vortex sheets with surface tension. Early works, such as the ones by Pullin [37], Rangel and Siringano [38], Baker and Moore [2], report difficulties with a numerical sawtooth instability which is suppressed using some form of ad-hoc smoothing, for example by point repositioning. Beale et al. [5–7] and Baker and Nachbin [3], studied the instability of spatial discretizations analytically and numerically, and proposed alternative stable methods. These works show that numerical instability arises generically due to an incompatibility in the discretization of the spatial derivatives and the singular integrals in the equation of motion.

In addition to the difficulty caused by numerical instability, surface tension introduces stiffness into the equations nonlinearly, through a product of high derivatives that contributes nonlocally to the vortex sheet motion. As a result, explicit schemes require a stringent timestep relative to the spatial discretization. For the vortex sheet problem considered here, the constraint is that $\Delta t \leqslant C\Delta s_{\min}^{3/2}$, where $\Delta s_{\min}$ is the smallest distance between points. This restriction can be removed using implicit schemes, although at a high computational cost in view of the nonlinearity. Much progress in resolving this issue came with the work of Hou et al. [19] (henceforth HLS, see also review paper [21]). Following previous researchers [18,22,29,45], they used a formulation based on the relative spacing between points s_α and the tangent angle θ, instead of the more standard formulation based on Cartesian coordinates x and y. This enabled them to determine the dominant term at small spatial scales responsible for stiffness, which turns out to be nonlocal, but linear. For periodic problems on a uniform mesh it diagonalizes under the Fourier Transform, which makes it possible to treat it implicitly at no additional cost, and thereby remove the stiffness constraint on the timestep. This approach, called the small scale decomposition, has been successfully implemented to resolve planar and axisymmetric vortex sheet evolution with surface tension, both for inertial sheets (HLS, [20,30]) and flows driven by Darcy's law (HLS, [10,11]). Ceniceros and Hou [9] show that the resulting semi-implicit scheme yields convergent results, as long as numerical filtering is carefully applied to insure stability. The above referenced papers use a Fourier filter. Unfortunately, the small scale decomposition does not trivially extend to nonperiodic problems and becomes computationally expensive for nonuniform meshes [20].

For axisymmetric vortex sheets there is an additional difficulty in accurately computing the vortex sheet velocity near the axis of symmetry [14]. The problem stems from singular behaviour of the integrands describing the velocity at points approaching the axis of symmetry. The integrands develop unbounded derivatives at the endpoints of the interval of integration, leading to loss of accuracy in their numerical evaluation [1,32]. This problem has been addressed both by Nie and Baker [31] using local mesh refinement, and by Nitsche [32] using asymptotic approximations of the relevant integrands, and both of these methods have been successfully implemented [11,30,33]. In this paper, we compute the axisymmetric sheet velocity using the latter approach.

The numerical works most closely related to the present one are by Nie [30] (henceforth Nie) and Lepinnen and Lister [27] (henceforth LL). Nie uses the small scale decomposition on a uniform mesh to compute planar and axisymmetric vortex sheet evolution, for the case of zero density jump across the sheet. He considers two initial conditions, one symmetric and one asymmetric about the plane $z = 0$, and studies the effect of the surface tension parameter. He finds that for small surface tension, the sheet pinches at a point away from the axis, for large surface tension it does not pinch at all, and for intermediate values, the symmetric sheet pinches at two points on the axis, leading to disconnection similar to the one observed in experiment. Nie refines the mesh by doubling the number of meshpoints a few times as pinchoff is approached, but the constraint to uniform grid spacing precludes full resolution of the disconnection process. LL compute the evolution from a different initial condition for a range of density jumps. They use an alternative computational method based on a formulation in cylindrical coordinates and the vortex dipole strength, and do not include any numerical filters. Local mesh refinement is obtained by repositioning the computational meshpoints at each timestep along quintic spline interpolants, so that the local grid spacing remains proportional to the distance of each grid point from the point of minimum radius that develops near pinchoff. Using this method, LL resolve the space-time neighbourhood of pinchoff and report self-similar behaviour as pinchoff is approached. They also solve steady equations in self-similar coordinates to obtain the self-similar shapes for a range of density jumps.

Here, we resolve vortex sheet pinchoff for the initial condition found by Nie to yield results similar to experimental observation. The numerical method is based on the s_α–θ formulation. Since the small scale decomposition is too computationally expensive for nonuniform meshes, it is not applied here, and therefore $\Delta t \leqslant C\Delta s_{\min}^{3/2}$ is required. However, this constraint proves not to be too costly and high resolution results can be obtained. A main contribution of this work is to introduce a new method to redistribute the computational meshpoints dynamically, so that they cluster at a desired point, in our case in the region of high curvature. This is achieved by imposing an evolution equation for the relative spacing between points, s_α, whose minimum value and position change in time. The minimum position moves continuously with the region of high curvature and the minimum value decreases in time to a prescribed value. Numerical tests confirm that this mesh refinement technique does not introduce artifacts near pinchoff and that the results converge as the number of meshpoints increases. The present results are compared to results by LL, showing agreement in the self-similar structures near pinchoff and in the tongues that develop for large Atwood number. New results include details about the cone–crater structure near pinchoff, and the dependence of satellite bubble volume and pinchoff time on the density jump.

The paper is organized as follows. Section 2 presents the governing equations, including the evolution equation for s_α used for mesh refinement. Section 3 describes the numerical method used to solve the governing equations. Section 4 presents the numerical results for a range of density jumps. The main results are summarized in Section 5.

2. Problem formulation

2.1. Governing equations

Vortex sheet evolution is governed by the boundary integral formulation introduced in Baker et al. [1]. That paper and the one by Shelley and Vinson [42] present two alternative derivations for the case of zero surface tension, with nonzero density jump across the sheet. Here, we choose to treat the nonzero surface tension case following the steps in [42].

The sheet is described by a curve in the symmetry plane, $\mathbf{x}(\alpha,t)=(r(\alpha,t),z(\alpha,t))$, $\alpha\in[0,\pi]$, where the z-axis is the symmetry axis, r is the radial direction, and α is a Lagrangian parameter that remains constant on computational particles. In the case considered in this work, the sheet is closed and separates interior fluid from exterior fluid. The fluid is described by its velocity $\mathbf{u}_{1,2}$, pressure $p_{1,2}$ and density $\rho_{1,2}$, where subscripts 1 and 2 refer to the inner and outer fluid, respectively, see Fig. 1(a). The arrows shown in the figure indicate the direction of increasing α. The fluid velocity on either side satisfies the incompressible Euler equations with the following boundary conditions:

$$[\mathbf{u}]\cdot\mathbf{n}=0 \quad \text{(kinematic boundary condition)}, \tag{2.1a}$$

$$[p]=\tau\kappa,\ \tau>0 \quad \text{(Laplace–Young condition)}, \tag{2.1b}$$

$$\mathbf{u}_j \to 0 \quad \text{as } r^2+z^2 \to \infty, \quad j=1,2 \quad \text{(vanishing far-field velocity)}, \tag{2.1c}$$

where $[f]=f_1-f_2$, and f_1, f_2 are the limiting values from inside and outside the bubble, $\mathbf{n}$ is the outward normal unit vector and κ is the median curvature

$$\kappa = \frac{\kappa_r+\kappa_z}{2}. \tag{2.2}$$

The components κ_z and κ_r, given by (1.1), are the principal curvatures of the surface in a cross-section with the r–z plane and a plane normal to it, respectively, with magnitude as indicated in Fig. 1(b).

The kinematic boundary condition states that the normal velocity component is continuous across the sheet. The tangential component may be discontinuous. The vortex sheet strength measures the tangential velocity jump across the sheet and is defined as

$$\gamma(\alpha) = -[\mathbf{u}]\cdot\mathbf{s} = (\mathbf{u}_2-\mathbf{u}_1)\cdot\mathbf{s}, \tag{2.3}$$

where $\mathbf{s}=\langle r_\alpha, z_\alpha\rangle/s_\alpha$ is the unit tangent vector and $s_\alpha=\sqrt{r_\alpha^2+z_\alpha^2}$ measures changes in arclength relative to changes in the parameter α. Concerning the notation, here and throughout this paper subscripts s, α or t denote differentiation with respect to those variables. (Other subscripts, such as r or z, do not denote differentiation.)

The Laplace–Young condition specifies the jump in pressure across the sheet as a function of curvature. Here, we assume that the surface tension $\tau>0$ is constant across the sheet. The sign of the pressure jump is such that for a sphere, the pressure is larger in the interior.

The third condition together with the Biot–Savart law and the Plemelj formulae implies that the average of the velocities on either side of the interface is

$$\left(\frac{\mathrm{d}\mathbf{x}}{\mathrm{d}t}\right)_{\mathrm{av}} = \frac{\mathbf{u}_1+\mathbf{u}_2}{2} = \mathbf{W}(\alpha,t) = \frac{1}{r}\mathrm{PV}\int_0^\pi \left(\frac{\partial\psi}{\partial\tilde{r}}, -\frac{\partial\psi}{\partial\tilde{z}}\right)\gamma(\tilde{\alpha})\,\mathrm{d}\tilde{\alpha}, \tag{2.4a}$$

where

$$\psi(r,z,\tilde{r},\tilde{z}) = \frac{r\tilde{r}}{4\pi}\int_0^{2\pi}\frac{\cos\theta}{\rho}\,\mathrm{d}\theta, \tag{2.4b}$$

$\rho^2=(z-z')^2+r^2+r'^2-2rr'\cos\theta$, $(r,z)=(r(\alpha,t),z(\alpha,t))$, $(\tilde{r},\tilde{z})=(r(\tilde{\alpha},t),z(\tilde{\alpha},t))$, and PV denotes the principal value of the integral. Thus,

$$\mathbf{u}_1 = \mathbf{W}-\frac{\gamma}{2}\mathbf{s}, \quad \mathbf{u}_2 = \mathbf{W}+\frac{\gamma}{2}\mathbf{s}. \tag{2.5}$$

Note that in practice, the integrands in (2.4a) are rewritten and evaluated in terms of elliptic integrals (e.g., see [32,33] for details).

The vortex sheet motion is independent of its tangential velocity component. Therefore, the vortex sheet velocity can be defined to be

$$\frac{\mathrm{d}\mathbf{x}}{\mathrm{d}t} = \left(\frac{\mathrm{d}r}{\mathrm{d}t},\frac{\mathrm{d}z}{\mathrm{d}t}\right) = \mathbf{u} = \mathbf{W}+T\mathbf{s}, \tag{2.6}$$

where T is arbitrary. As suggested by HLS, we will choose T to control the clustering of numerical particles along the interface.

Eq. (2.6) gives evolution equations for the cylindrical variables r and z. The evolution equation for the remaining independent variable, γ, can be obtained from the Euler equations on either side of the interface, written in a frame moving with velocity $\mathbf{u}$:

$$\rho_1 \frac{\partial \mathbf{u}_1}{\partial t} + \rho_1[(\mathbf{u}_1 - \mathbf{u}) \cdot \nabla]\mathbf{u}_1 + \nabla p_1 = 0, \tag{2.7a}$$

$$\rho_2 \frac{\partial \mathbf{u}_2}{\partial t} + \rho_2[(\mathbf{u}_2 - \mathbf{u}) \cdot \nabla]\mathbf{u}_2 + \nabla p_2 = 0, \tag{2.7b}$$

where body forces have been neglected and the gradient is taken with respect to the new variable $\xi(\alpha, t) = \mathbf{x}(\alpha, t) - \int_0^t \mathbf{u}(\alpha, \tilde{t})\,\mathrm{d}\tilde{t}$. The convective term in (2.7) follows from the fact that in the limit from within the bubble, $(\mathrm{d}\mathbf{x}/\mathrm{d}t) = \mathbf{u}_1$ and

$$\frac{\mathrm{d}}{\mathrm{d}t} = \frac{\partial}{\partial t} + \frac{\mathrm{d}\xi_i}{\mathrm{d}t}\frac{\partial}{\partial \xi_i} = \frac{\partial}{\partial t} + \left(\frac{\mathrm{d}x_i}{\mathrm{d}t} - u_i\right)\frac{\partial}{\partial \xi_i} = \frac{\partial}{\partial t} + \left(\frac{\mathrm{d}\mathbf{x}}{\mathrm{d}t} - \mathbf{u}\right) \cdot \nabla_\xi = \frac{\partial}{\partial t} + (\mathbf{u}_1 - \mathbf{u}) \cdot \nabla_\xi$$

and similarly outside the bubble. Following the steps outlined by Shelley and Vinson [42], one can show that under the assumption that $\rho_{1,2}$ are constant, the difference between equations (2.7a) and (2.7b) is equivalent to

$$\frac{\partial \gamma}{\partial t} + (\gamma \mathbf{W}_s \cdot \mathbf{s} - T\gamma_s) = -2A\left(\frac{\partial \mathbf{W}}{\partial t} \cdot \mathbf{s} - T\mathbf{W}_s \cdot \mathbf{s} + \frac{1}{8}(\gamma^2)_s\right) + \frac{\tau \kappa_s}{\rho_{\mathrm{av}}}, \tag{2.8}$$

where $A = (\rho_2 - \rho_1)/(\rho_2 + \rho_1)$ is the Atwood number and $\rho_{\mathrm{av}} = (\rho_1 + \rho_2)/2$. This is the evolution equation for γ. The governing equations therefore are (2.6) and (2.8) for the variables r, z, γ. The initial condition of interest here is the spherical sheet

$$r(\alpha, 0) = \cos(\alpha), \quad z(\alpha, 0) = \sin(\alpha), \quad \gamma(\alpha, 0) = 2\sin 2\alpha, \quad \alpha \in [0, \pi], \tag{2.9}$$

with surface tension parameter $\tau/\rho_{\mathrm{av}} = 0.2$. These are the conditions for which Nie obtained results similar as observed in experiment. Note that the surface tension value is dimensional, and is not in the small surface tension regime, but is one of the intermediate surface tension values studied by Nie.

2.2. Alternative formulation

The first works regarding interfacial flow with surface tension studied numerical solutions to equations formulated in Cartesian or cylindrical coordinates, such as (2.6) and (2.8), and found that the discretizations are unstable (e.g., [2,37,38]). Later Beale et al. [5,6] and Baker and Nachbin [3] showed that the instability arises generically due to an incompatibility in the discretization of the spatial derivatives and the singular integrals in the equation of motion.

The governing equations can alternatively be reformulated as proposed in HLS, by replacing the independent variables r, z, γ by the relative spacing between points s_α, the tangent angle θ, and a scaled vortex sheet strength $\tilde{\gamma}$, where

$$\tilde{\gamma} = \gamma s_\alpha. \tag{2.10}$$

New variables $\widetilde{U}, \widetilde{T}$ are also introduced, defined by

$$\mathbf{x}_t = \widetilde{U}\mathbf{n} + \widetilde{T}\mathbf{s}, \tag{2.11}$$

where $\mathbf{n} = \langle -z_\alpha, r_\alpha \rangle / s_\alpha$ is a unit vector normal to the sheet and $\mathbf{s}$ is as before the unit tangent vector. It follows that $\widetilde{U} = \mathbf{W} \cdot \mathbf{n}$ and $\widetilde{T} = \mathbf{W} \cdot \mathbf{s} + T$. One can now show that (2.6) and (2.8) is equivalent to

$$s_{\alpha,t} = \widetilde{T}_\alpha - \theta_\alpha \widetilde{U}, \tag{2.12a}$$

$$\theta_t = \frac{1}{s_\alpha}(\widetilde{U}_\alpha + \widetilde{T}\theta_\alpha), \tag{2.12b}$$

$$\tilde{\gamma}_t = \left[(\widetilde{T} - \mathbf{W}\cdot\mathbf{s})\frac{\tilde{\gamma}}{s_\alpha}\right]_\alpha - 2A\left[s_\alpha \mathbf{W}_t\cdot\mathbf{s} + \frac{1}{8}\left(\left(\frac{\tilde{\gamma}}{s_\alpha}\right)^2\right)_\alpha - (\widetilde{T} - \mathbf{W}\cdot\mathbf{s})\mathbf{W}_\alpha\cdot\mathbf{s}\right] + \tilde{\tau}\kappa_\alpha, \tag{2.12c}$$

where $\kappa = \theta_s$ and $\tilde{\tau} = \tau/\rho_{\rm av}$ is a normalized surface tension. For the derivation of equations (2.12a) and (2.12b), see HLS. Eq. (2.12c) is equivalent to (2.8), after noting that $s_{\alpha,t} = \mathbf{W}_\alpha\cdot\mathbf{s} + T_\alpha$, which follows from the definition of s_α. In these variables, the initial condition (2.9) is

$$s_\alpha(\alpha,0) = 1, \quad \theta(\alpha,0) = \alpha, \quad \tilde{\gamma}(\alpha,0) = 2\sin(2\alpha). \tag{2.13}$$

Ceniceros and Hou [9] showed that just as in the Cartesian variables, discretizations using the s_α–θ formulation need to preserve a delicate balance among the most singular terms to ensure stability. Together with careful filtering and the small scale decomposition of HLS, Hou et al. [19,20] and Nie solved (2.12) and successfully resolved the vortex sheet motion.

2.3. Mesh refinement

Vortex sheet motion is most commonly computed by moving the computational particles with the average velocity $\mathbf{W}$, that is, by setting $T = 0$, or equivalently, $\widetilde{T} = \mathbf{W}\cdot\mathbf{s}$. That is not practical in the present case. To illustrate, Fig. 2 plots the position at $t = 1.7$ of particles initially uniformly distributed on the sphere (2.13) that have evolved with the average velocity using the method described in the next section. Fig. 2(a) plots a linear interpolant of the particles, showing that a region of high curvature has developed. Fig. 2(b) plots a closeup of the particles position, showing that in this case the high curvature region is underresolved since the particles do not cluster there, but at a nearby inflection point instead.

Several approaches have been taken to better resolve the region of high curvature. HLS choose $\widetilde{T}$ so that the particles remain uniformly spaced at all times. Nie uses this uniform mesh, but doubles the total number of particles a few times as the curvature increases, by placing new particles on spline interpolants of the existing ones, thus refining the mesh uniformly as the curvature increases. In LL, local mesh refinement is

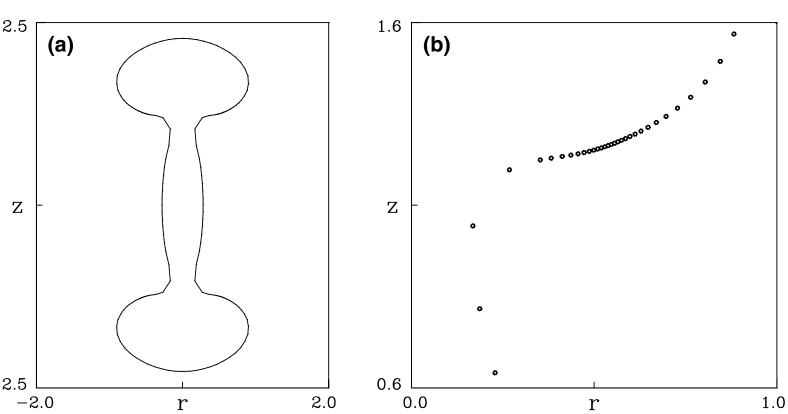

Fig. 2. Particle position at $t = 1.7$, computed using average velocity frame $\widetilde{T} = \mathbf{W}\cdot\mathbf{s}$, with 100 initially uniformly spaced points, for $A = 0$. (a) Linear interpolant of computational meshpoints. (b) Closeup showing meshpoint position.

achieved by repositioning the existing particles on a quintic interpolant at every time step so that the local grid spacing remains proportional to the distance of the particles to the point of minimal radius in the high curvature region.

The method chosen here is closest to an alternative proposed by HLS. They suggest to obtain local mesh refinement by specifying $\widetilde{T}$ so that the relative spacing between particles is $s_\alpha = R(\alpha)L(t)$, where L is the length of the curve and R has a minimum at a desired value of α. This approach, used in [20], implies that: (1) the particles cluster at a fixed position α_c at all times and (2) the amount of refinement is fixed in time. However, in the problem considered here the position of largest curvature moves in time, and the region of local refinement should ideally move with it. One would also like the points to be initially uniformly distributed and the amount of local refinement to increase as the curvature increases. To accomplish this, we set

$$s_\alpha = f(\alpha, t), \tag{2.14}$$

where $f > 0$ is specified dynamically to be smallest at the point where pinchoff develops, with decreasing minimum value, corresponding to increasing local refinement in time. The function f needs to satisfy the constraint

$$\int_0^\pi f \, \mathrm{d}\alpha = \int_0^\pi s_\alpha \, \mathrm{d}\alpha = L(t). \tag{2.15}$$

Once f is specified, $\widetilde{T}(\alpha, t)$ is determined from $s_{\alpha,t} = f_t(\alpha, t) = \widetilde{T}_\alpha - \theta_\alpha \widetilde{U}$ to be

$$\widetilde{T}(\alpha, t) = \widetilde{T}(0) + \int_0^\alpha f_t + \theta_\alpha \widetilde{U} \, \mathrm{d}\alpha', \tag{2.16}$$

where we choose $\widetilde{T}(0) = 0$. Note that in view of the symmetry of the initial conditions (2.13), $s_\alpha, \theta_\alpha, \tilde{\gamma}$, and therefore $\mathbf{W}$ and $\widetilde{U}$, are periodic with period π. To ensure that they remain so, $\widetilde{T}$ needs to be periodic as well. This is achieved by enforcing that f is periodic with

$$\int_0^\pi f_t \, \mathrm{d}\alpha = -\int_0^\pi \theta_\alpha \widetilde{U} \, \mathrm{d}\alpha. \tag{2.17}$$

In summary, dynamic mesh refinement is obtained by solving (2.12) with $\widetilde{T}$ as given in (2.16). The explicit formula we chose for f is presented in the next section. This mesh refinement formulation agrees with the one given by HLS when $s_\alpha = c(t)$ (uniformly spaced points) and $s_\alpha = R(\alpha)L(t)$ (fixed amount and position of refinement).

3. Numerical method

The numerical method consists of solving a discrete approximation to (2.12) and (2.16). It differs from the method used by Nie, introduced by HLS, in that it includes dynamic mesh refinement and does not incorporate the small scale decomposition, which is costly for nonuniform meshes. It differs from the method used by LL in that it uses the s_α–θ formulation instead of one in cylindrical coordinates and uses a different method for local mesh refinement.

3.1. Discretization and initial condition

The vortex sheet is discretized by $N + 1$ points uniformly spaced in the Lagrangian variable α, with values

$$s_{\alpha,j}(t) = s_\alpha(\alpha_j, t), \quad \theta_j(t) = \theta(\alpha_j, t), \quad \tilde{\gamma}_j(t) = \tilde{\gamma}(\alpha_j, t), \tag{3.1}$$

where $\alpha_j = j\pi/N,\ j = 0, \ldots, N$, and $s_{\alpha,j}(0) = 1,\ \theta_j(0) = \alpha_j,\ \tilde{\gamma}_j(0) = 2\sin(2\alpha_j)$.

3.2. Time integration

The discrete values are updated in time by solving (2.12) at the meshpoints using the fourth-order Runge–Kutta method. The method is stable as long as

$$\Delta t \leqslant C\Delta s_{\min}^{3/2}, \tag{3.2}$$

where $C = 2.5$ was found to be sufficiently small for stability. As noted earlier, the stiffness constraint (3.2) can be eliminated using the small scale decomposition proposed by HLS, but at a high computational expense if the mesh is nonuniform [20]. Furthermore, we reproduced some of Nie's simulations, which were computed with the small scale decomposition, using the present scheme without the decomposition, and found that the timestep required for stability here is the same as the final timestep required by Nie. This is consistent with results by Ceniceros and Hou [9], who examined a spatial and temporal discretization for a simple case and showed that the stability constraint of semi-implicit methods such as the one by HLS is linked to the curvature and regularity of the solution. Thus, for interfaces developing large curvatures the time step of the semi-implicit method must also be small, as the computations of Nie show. For these types of problems the explicit boundary integral methods may therefore be at least competitive with the implicit discretizations. We choose the explicit method, keeping the constraint (3.2), and gain accuracy using mesh refinement.

To approximate the right-hand side in (2.12), the following components are needed at each stage of the Runge–Kutta method:

(i) *Computing all spatial derivatives and integrals.* All spatial derivatives needed (as in the right-hand side of (2.12)) are computed using fourth-order centered finite differences, where the periodic extension about $r = 0$ is used to obtain fourth-order approximations at endpoints. All integrals (as in (2.15) and (2.16), and in (ii)–(iv) below) are evaluated to fourth-order accuracy using the trapezoid rule with a correction given by the first term in the Euler–McLaurin series for the error. The correction is given in terms of derivatives of the integrands at the endpoints, which are evaluated to at least second order using finite differences.

(ii) *Computing the velocity* **W**. To compute **W** one first needs to recover r, z from s_α, θ. This is done by integrating

$$r_\alpha = s_\alpha \cos\theta, \quad z_\alpha = s_\alpha \sin\theta \tag{3.3}$$

as explained in (i).

The principal value integrals in (2.4a) are computed using the fifth-order quadrature rule described in Nitsche [33]. This quadrature rule is uniformly accurate for all points, and removes the loss of resolution previously observed near the axis of symmetry (also see [1,14,31,32]).

(iii) *Computing* $s_{\alpha,t} = f_t$ *and* $\widetilde{T}$. The function $s_{\alpha,t} = f_t$ is determined so that the relative spacing between points $s_\alpha = f$ gives the desired point distribution. To satisfy condition (2.15), we write $f = R(\alpha, t)L(t)$ where $\int_0^\pi R\,\mathrm{d}\alpha = 1$ and L is the length of the curve. The function $R(\alpha, t)$ is chosen to be initially constant in α, and later develop a minimum near the points leading to pinchoff. Because of symmetry, there are two such points at $\alpha = \alpha_c, \pi - \alpha_c$. The values for α_c, computed dynamically during the simulation, should evolve continuously in time towards pinchoff. Two definitions of α_c that satisfied this condition were used: either the value at which the tangential velocity $\mathbf{W} \cdot \mathbf{s}$ attains a minimum (used for $A \leqslant 0.6$), or the value at which $\theta = 3\pi/2$ near the point of minimal radius, once it has established (used for $A = 0.7$). Both of these definitions coincide at later times with the point of maximal curvature. The point of maximal curvature was not a good parameter since its position jumps discontinuously at early times.

The guidelines taken to choose $R(\alpha,t)$ are: R should be a positive function that depends on a parameter ϵ so that when $\epsilon=0$ the function is constant (corresponding to a uniform mesh) and for $0<\epsilon<1$ it has two symmetric minima at $\alpha_c, \pi-\alpha_c$, with decreasing minimum value as ϵ increases. Furthermore, to preserve the periodicity of all variables, R needs to be periodic as well. The function

$$g(x) = 1.125 + \epsilon(\cos(4x) - \cos(2x)), \quad \text{where } x = \pi\left(\frac{s(\alpha)}{L} - 0.5\right), \tag{3.4}$$

shown in Fig. 3(a), satisfies many of these conditions. It is periodic, it is constant if $\epsilon=0$ and it has a positive minimum of $1.125(1-\epsilon)$ at two symmetric points if $0<\epsilon<1$. However, the minima occur at fixed points $\pm x_0, x_0=\cos^{-1}(0.25)/2$. Since we wish to specify the position of the minima arbitrarily to be at $s(\alpha_c)$, $\pi - s(\alpha_c)$, we need to compose $g(x)$ with a monotonically increasing function $p(x)$ that maps $x_{\min}=\pi(s(\alpha_c)/L-0.5)$ to $-x_0$ and $\pi - x_{\min}$ to x_0. To preserve the periodicity of $g(x)$, it is necessary that $p(\pm\pi/2)=\pm\pi/2$ and that the derivative $p'(x)$ and all higher derivatives be periodic. The function

$$p(x) = \tan^{-1}(b\tan x), \quad b = \tan(-x_0)/\tan(x_{\min}) \tag{3.5}$$

satisfies all these requirements. It is plotted in Fig. 3(b) for a range of values $x_{\min}$ corresponding to $0.1 \leqslant \mathbf{s}(\alpha_c)/L \leqslant 0.45$. The points $(x_{\min}, -x_0), (\pi - x_{\min}, x_0)$ are indicated by a cross. Finally, since R is to have integral 1, the resulting composition $g(p)$ is divided by its total integral. While other choices are surely possible, the formula for R that we used as a result of these considerations is

$$R(\alpha,t) = \frac{g(p)}{\int_0^\pi g(p)\,\mathrm{d}\alpha} \tag{3.6}$$

shown in Fig. 3(c), for the same range of values $x_{\min}$ as in Fig. 3(b). The arclength parameter $s(\alpha)$ needed to compute g is obtained by integrating s_α to fourth order, as described in (i).

The parameter ϵ (see (3.4)) measures the deviation of R from the constant; $\epsilon=0$ corresponds to constant R and thus to uniformly distributed points, $\epsilon=1$ corresponds to a function R with zero minimum value. We choose ϵ to increase linearly from 0 to some maximum value $\epsilon_{\max}$ just below 1, attained at $t=t_c$,

$$\epsilon = \epsilon_{\max}\frac{t}{t_c}, \tag{3.7}$$

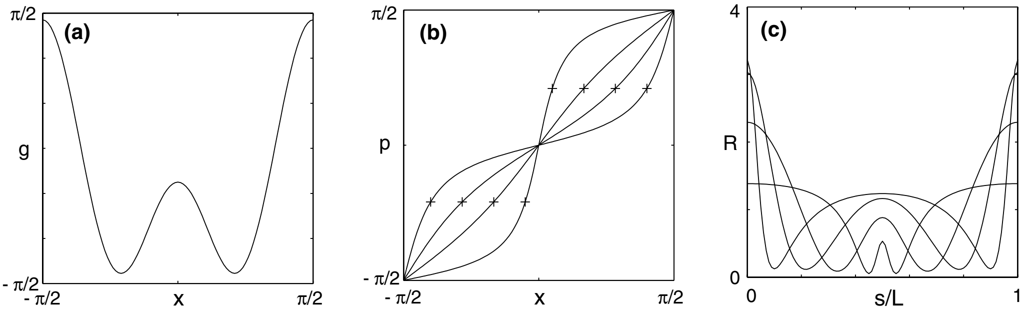

Fig. 3. Construction of $R(\alpha,t)$, for $\epsilon=0.9$ and a range of values $0.1 \leqslant s(\alpha_c)/L \leqslant 0.45$. (a) The function $g(x)$. (b) The function $p(x)$ mapping $x_{\min}=\pi(s(\alpha_c)/L-0.5)$ to x_0. The points $(x_{\min},x_0)$ are marked by an 'x'. (c) Normalized composition R vs. arclength s/L.

where t_c and $\epsilon_{\max}$ are user specified parameters. The parameter t_c is typically chosen to be a value slightly larger than the estimated pinchoff time t_{p}, so that always $\epsilon < 1$. The parameter $0 \leqslant \epsilon_{\max} < 1$ determines the amount of final mesh refinement, with no mesh refinement if $\epsilon_{\max} = 0$ and increasing refinement as $\epsilon_{\max} \to 1$.

Once R is specified, the derivative f_t is computed from

$$f_t = R_t L + R L_t, \quad \text{where } L_t = -\int_0^{\pi} \theta_\alpha \widetilde{U}\, \mathrm{d}\alpha. \tag{3.8}$$

This equation ensures that condition (2.17) is satisfied. R_t is approximated with first-order finite differences using the value of R at the previous timestep. The accuracy in evaluating R_t has essentially no effect on the overall accuracy of the method and solely affects the position of the points, which satisfies $s_\alpha \approx f$ at all times. Once f_t is determined, $\widetilde{T}$ is determined from (2.16).

(iv) *Computing* $\tilde{\gamma}_t$ *for* $A \neq 0$. For $A \neq 0$, Eq. (2.12c) is a Fredholm integral equation for $\tilde{\gamma}_t$, since $\mathbf{W}_t = (\mathrm{d}/\mathrm{d}t)\int G\tilde{\gamma} = \int G_t\tilde{\gamma} + \int G\tilde{\gamma}_t$ depends on $\tilde{\gamma}_t$. The quantity G_t is approximated numerically and the resulting equation is

$$\tilde{\gamma}_t = \int G\tilde{\gamma}_t \, \mathrm{d}\alpha + \mathrm{rhs}, \tag{3.9}$$

where rhs is independent of $\tilde{\gamma}_t$, is solved using GMRES [40].

3.3. Filtering

The vortex sheet is subject to the Kelvin–Helmholtz instability. In the absence of surface tension, high wave number Fourier modes introduced by roundoff error at the level of machine precision grow exponentially fast. This problem is usually avoided using a Fourier filter introduced by Krasny [26]. Surface tension damps the growth of high wavenumber modes. The present computations were performed with 14 digits of precision and normalized surface tension $\tau/\rho_{\mathrm{av}} = \tilde{\tau} = 0.2$, and this amount of surface tension was found to damp errors at the level of machine precision in most cases without requiring filtering.

However, another source of roundoff error much larger than machine precision occurs when computing derivatives of κ_r, needed in (2.12c), near points on the axis, $s = 0, L$. Near these points, κ_r (see Eq. (1.1)) is a quotient of two numbers that vanish as $r \to 0$. Computing the derivative of this quotient introduces large noise that grows under the Kelvin–Helmholtz or the sawtooth instability of the sheet. The noise, created at the endpoints, travels into the interior of the domain and contaminates the solution. Several approaches are considered to prevent this.

(i) *Krasny's Fourier filter.* One possibility is to apply Krasny's Fourier filter, in which the noise is smoothed by removing all Fourier modes in the solution below a certain filter level at each timestep. The chosen filter level here was 10^{-11} or smaller. However, this filter level was not always sufficient to eliminate the errors introduced at the endpoints.

(ii) *Viscosity near endpoints.* Another possibility is to add a small amount of viscosity to a region near the boundary. We chose to replace κ_s by $\kappa_s + \nu\Delta\kappa_s$ in a small region near the endpoints, where ν varies continuously from 0 (in inner boundary of region) to a value $\nu_{\max}$ (at endpoints), where $0.0001 \leqslant \nu_{\max} \leqslant 0.001$.

(iii) *Alternative computation of* $\kappa_{r,s}$ *near endpoints.* A third possibility is to use the fact that near $s = 0$, and similarly near $s = L$, derivatives of κ_r can be expressed in terms of derivatives of κ_z, using the relation

$$\kappa_{r,s}(s) = \kappa_{z,s}(s)/3 + \mathrm{O}(s^3) \tag{3.10}$$

proven in Appendix A. Since $\kappa_{z,s}$ can be computed accurately near the axis, this relation enables one to smoothly approximate $\kappa_{r,s}$ near the axis. We choose to approximate

$$\kappa_{r,s}(s) \approx \beta(s)\kappa_{r,s}(s) + (1-\beta(s))\kappa_{z,s}(s)/3, \tag{3.11}$$

where $\beta(s)$ is an odd, twice continuously differentiable function with $\beta(s) = 1$ if $s > 0.1$, $\beta(0) = 0$, and given by a seventh-order polynomial for $0 < s < 0.1$.

None of these three approaches by themselves was successful in all cases, although each was successful by themselves in some cases. The Fourier filter with level $\leqslant 10^{-11}$ was applied to all cases $A \leqslant 0$. For $A > 0$, either the second or third approach was used, either individually or in addition to the Fourier filter. The results reported here are independent of which of these methods was used, as long as the method used was successful in removing the noise introduced at the endpoints. We note that the difficulty requiring some form of filter is attributed primarily to errors introduced at the axis and is not expected to occur if these errors are absent (for example, in planar flow or if the sheet does not touch the axis).

4. Numerical results

4.1. Evolution for $A = 0$

Fig. 4 plots the solution $(r(\alpha,t), z(\alpha,t))$, $\alpha \in [0,\pi]$, at the indicated times, for the equal density case $A = 0$ computed with $N = 4000$, $\epsilon_{\max} = 0.99$. The image $(-r(\alpha,t), z(\alpha,t))$ is also plotted, thus showing a cross-section of the axisymmetric surface in the symmetry plane. As mentioned, the initial condition is the spherical sheet (2.13) and the surface tension parameter is $\tilde{\tau} = \tau/\rho_{\text{av}} = 0.2$. At $t = 1$, the sheet has developed a barbelled shape that preserves the initial symmetry about $z = 0$. At $t = 1.7$, two symmetric neck regions have formed, one for $z > 0$ and one for $z < 0$, in which the radius has a local minimum. The minimum radius, the half-width of the neck, decreases in time and shrinks to zero at a finite time t_{p} slightly larger than the last time shown, $t = 1.89518$. As a result, the sheet pinches at two points, separating two symmetric bubbles at the top and bottom from a satellite bubble in between. Notice that near the pinchoff point, the top and bottom bubbles fold into themselves, forming a so-called crater, while the middle bubble takes the shape of a cone. The resulting pinchoff structure is therefore referred to as a cone–crater structure. Also note that near the pinchoff time (for example, at $t = 1.7$), the curvature κ_z changes sign on both the crater

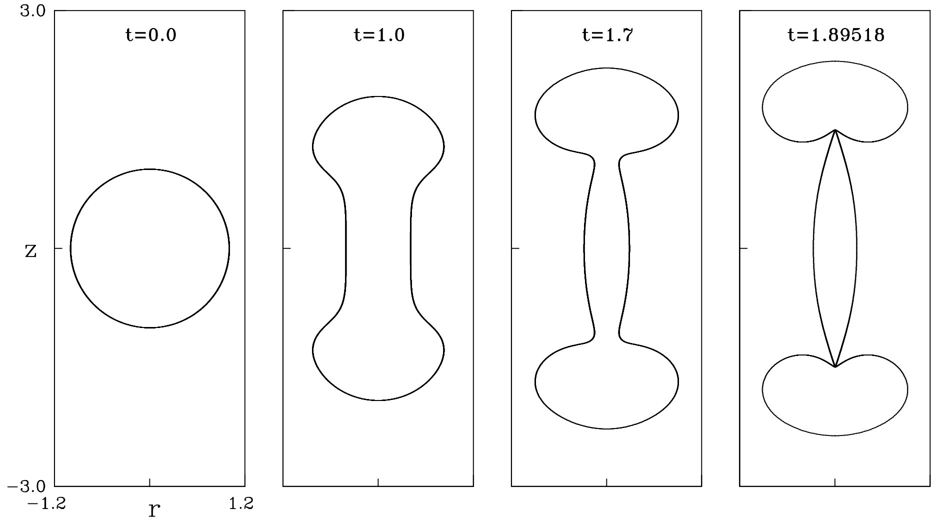

Fig. 4. Bubble interface for $A = 0$ at the indicated times, computed with $N = 4000$, $\epsilon_{\max} = 0.99$.

and the cone branch, leading to one inflection point on each branch. The evolution of these inflection points as pinchoff is approached will be addressed later.

A closeup of the evolution towards pinchoff is illustrated in Fig. 5, which plots the solution at a sequence of times $t \in [1.88, 1.89518]$. It shows the minimum radius decreasing to zero, and the position of the neck approaching a limit point $(0, z_0)$ on the z-axis. At the pinchoff time, the curvature at the point of minimal radius is unbounded and cannot be resolved. The last time plotted here is the last time at which the solution remains resolved.

Fig. 6 plots the corresponding evolution of the variables s_α, θ, γ, and of the associated curvatures κ_z, κ_r, at the indicated times, as functions of s/L. Here s is the arclength parameter and L is the total length of the curve $(r(\alpha, t), z(\alpha, t)), \alpha \in [0, \pi]$. All functions are symmetric about $s/L = 0.5$ because of the symmetry of the problem about $z = 0$. The figure shows the discrete values at the computational meshpoints for $s/L < 0.5$, and an interpolating curve for $s/L > 0.5$.

The relative spacing between points s_α, plotted in Fig. 6(a), is dynamically determined in the code by specifying $s_{\alpha,t} = f_t$, as described in Section 3.2(ii). The figure shows that initially, s_α is constant (equal to $L/\pi = 1$), corresponding to uniformly spaced points. At later times, s_α develops a minimum at a point which continuously evolves towards the pinchoff point. The minimum value decreases in time, corresponding to continuous mesh refinement near this point. At the same time, the maximum value at $s/L = 0, 1$ increases, corresponding to mesh coarsening near the endpoints. The point distribution at the final time $t = 1.89518$ is indicated in Fig. 7, which, for clarity, plots the position of every 10th computational point only. At this time, the finest spacing between points is $L/50,000$. For reference, the spacing using a uniform mesh with the given value of N would have been $L/4000$.

The tangent angle θ, plotted in Fig. 6(b), develops a jump at the pinchoff point, corresponding to a corner in the vortex sheet. The discrete data shown for $s/L < 0.5$ indicates roughly the number of points across the jump. Notice that on both sides of the jump the angle θ attains a local extremum. These local extrema correspond to the inflection points in the curve $(r(\alpha, t), z(\alpha, t))$ mentioned earlier.

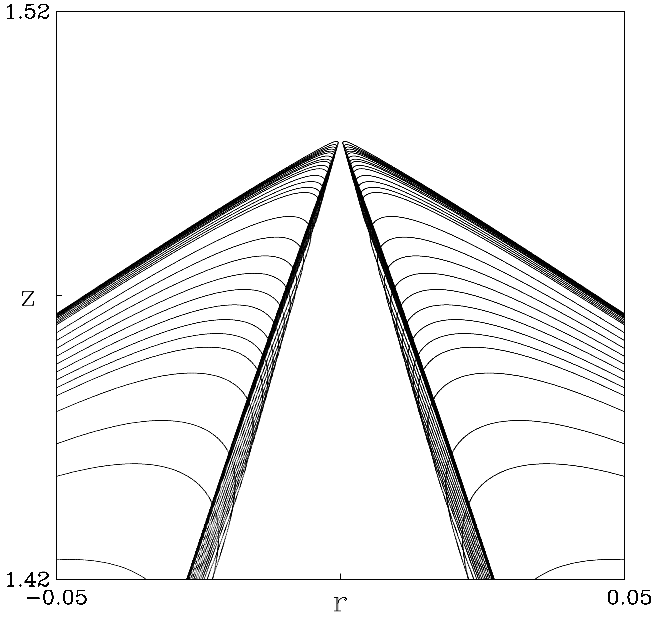

Fig. 5. Solution near pinchoff for $A = 0$, $N = 4000$, $\epsilon_{\max} = 0.99$, at a sequence of times $t \in [1.88, 189518]$.

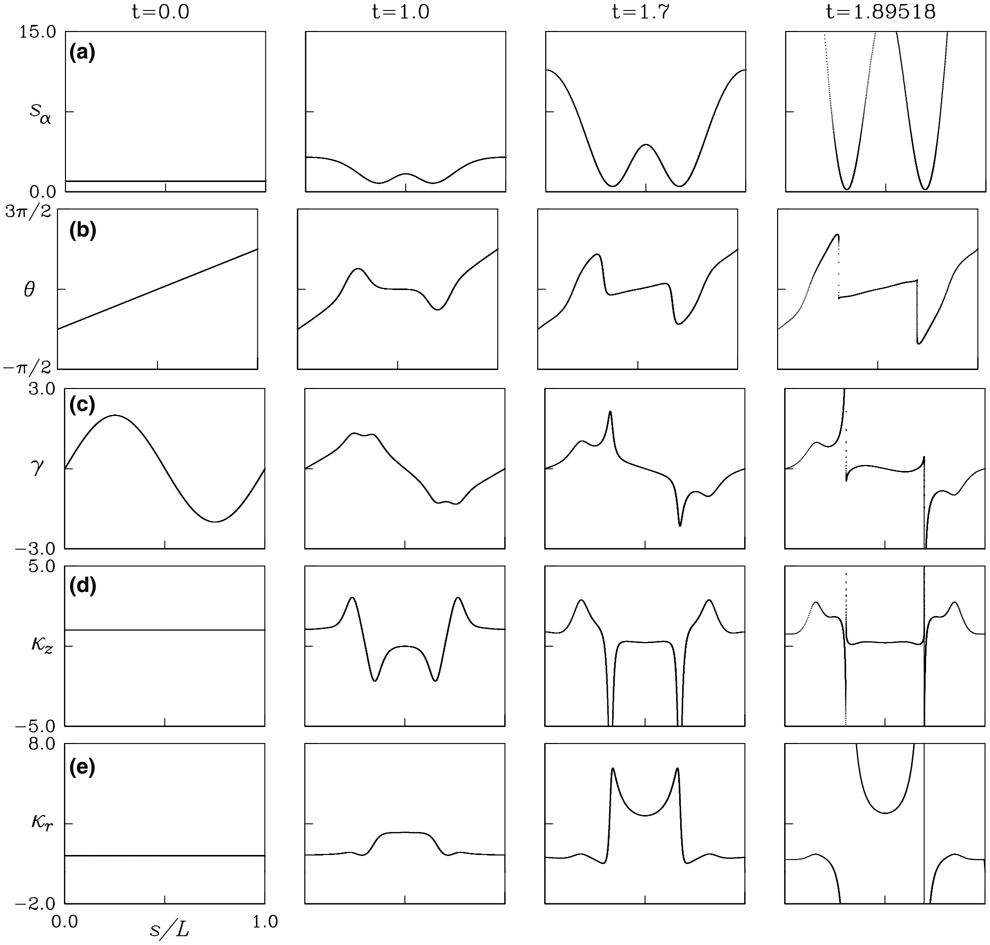

Fig. 6. (a) Relative spacing s_α, (b) tangent angle θ, (c) vortex sheet strength γ, (d,e) principal curvatures κ_z, κ_r, at the indicated times, vs normalized arclength s/L, for $A = 0$, $N = 4000$, $\epsilon_{\max} = 0.99$.

The vortex sheet strength γ, plotted in Fig. 6(c), is the jump in the tangential velocity component. We note that other authors have plotted $\tilde{\gamma} = \gamma s_\alpha$, while we choose to plot γ since it does not depend on the point distribution. The figure shows that γ becomes unbounded at pinchoff. At the final time plotted, the maximum sheet strength is $\gamma_{\max} \approx 36$.

Both the principal curvatures κ_z and κ_r, plotted in Figs. 6(d) and (e), also become unbounded at pinchoff. At the last time shown, their absolute maxima are $|\kappa_z|_{\max} \approx 3100$ and $|\kappa_r|_{\max} \approx 1580$. As pinchoff is approached the maxima increase and resolution is lost, leading to noise in all variables. All the runs presented in this paper are only shown for those times at which they are still resolved and no noise is visible.

4.2. Self-similar collapse, $A = 0$

The inviscid pinchoff process is expected to be self-similar. Theoretical arguments based on balancing the dynamic and capillary pressure terms under the assumption that r and $z - z_0$ have comparable length scales near pinchoff lead to the similarity scaling ([13,15], LL),

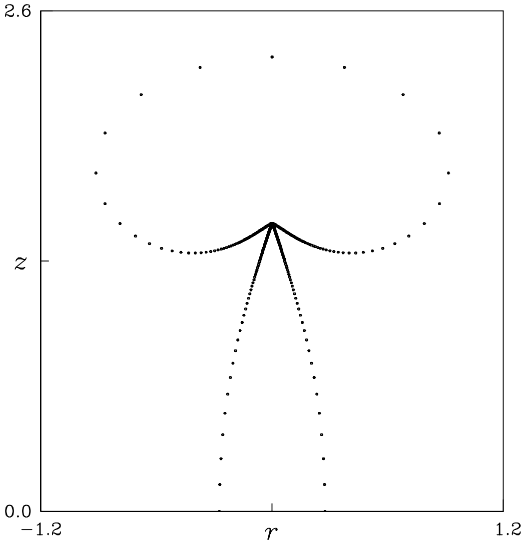

Fig. 7. Position of every 10th computational point (r_j, z_j), $j = 0{:}10{:}N$ at $t = 1.89518$, for $A = 0$, $N = 4000$, $\epsilon_{\max} = 0.99$.

$$r, z - z_0 \sim (t_{\mathrm{p}} - t)^{2/3}. \tag{4.1}$$

This scaling has been observed both in [13] for $A = 0$ and in LL for $A \neq 0$, for different initial conditions. To test the extent to which (4.1) holds in the present case, Fig. 8 plots $r_{\min}^{3/2}$ vs t (discrete data), where $r_{\min}$ is the minimum radius in the neck region. Fig. 8(b) is a closeup of Fig. 8(a). As $r_{\min} \to 0$, the data are well approximated by the line shown. This shows that the scaling (4.1) is well satisfied and gives an estimate for $t_{\mathrm{p}} = 1.89523$. To determine the accuracy of these results, the figure plots the results for $N = 4000, \epsilon_{\max} = 0.99$ (○), $N = 2000, \epsilon_{\max} = 0.99$ (×), and $N = 4000, \epsilon_{\max} = 0$ (+) (corresponding to no local refinement), for those times at which no noise is visible. The fact that all three datasets are practically indistinguishable gives strong evidence that the results have converged.

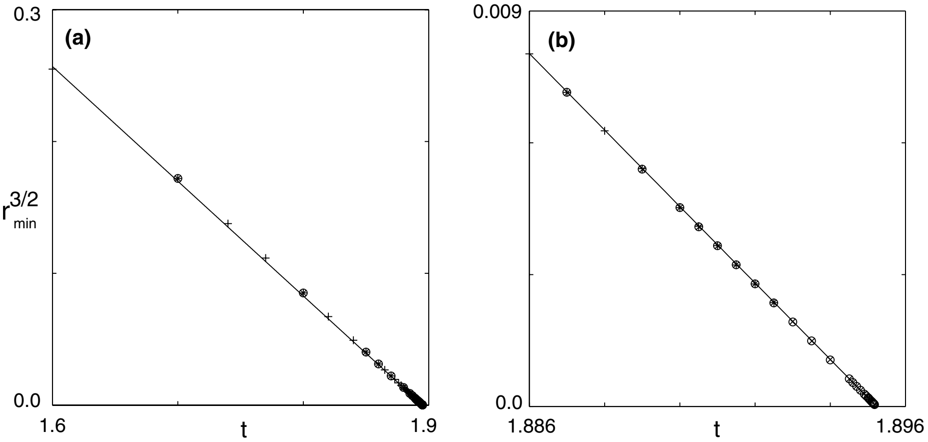

Fig. 8. $r_{\min}^{3/2}$ vs t, where $r_{\min}$ is the minimum radius in the neck region. The results for $N, \epsilon_{\max} = 4000, 0.99$ (○), $N, \epsilon_{\max} = 2000, 0.99$ (×), $N, \epsilon_{\max} = 4000, 0.00$ (+) are shown, and a line that approximates the data as $r_{\min} \to 0$. (b) is a closeup of (a).

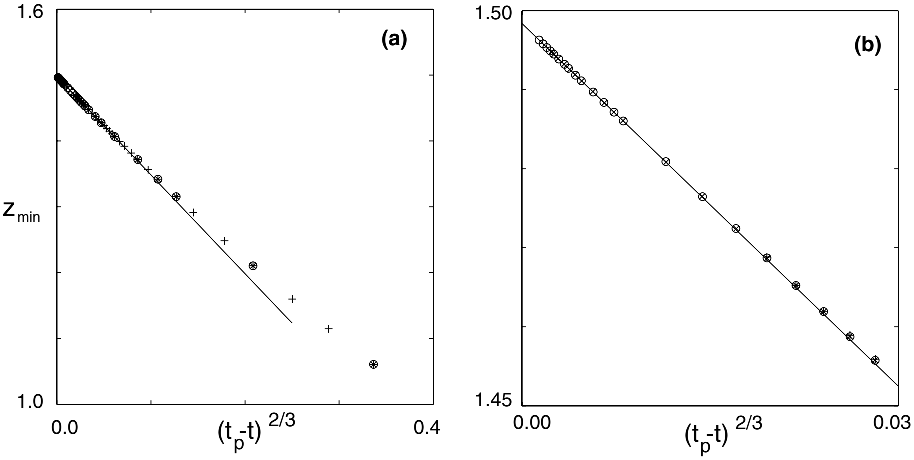

Fig. 9. $z_{\min}$ vs $(t_p - t)^{2/3}$, where $z_{\min}$ is the z-coordinate of the point of minimal radius in the upper neck region. The results for $N, \epsilon_{\max} = 4000, 0.99$ (○), $N, \epsilon_{\max} = 2000, 0.99$ (×), $N, \epsilon_{\max} = 4000, 0.00$ (+) are shown, and a line that approximates the data as $t \to t_p$. (b) is a closeup of (a).

Having thus estimated t_p, Fig. 9 plots $z_{\min}$ vs $(t_p - t)^{2/3}$, where $z_{\min}$ is the z-coordinate of the point of minimal radius in the upper neck region. As before, Fig. 9(b) is a closeup of Fig. 9(a), and all results for $N = 4000, \epsilon_{\max} = 0.99$ (○), $N = 2000, \epsilon_{\max} = 0.99$ (×), and $N = 4000, \epsilon_{\max} = 0.0$ (+), are shown. The data are well approximated by the line shown, giving the estimate $z_0 = 1.49839$.

One can now plot the solution at a sequence of times in self-similar coordinates

$$r^* = \frac{r}{(t_p - t)^{2/3}}, \quad z^* = \frac{z - z_0}{(t_p - t)^{2/3}}. \tag{4.2}$$

Fig. 10(a) plots the solution (r^*, z^*) at the times $t_p - t$ indicated by the inset of Fig. 10(b). The values of $t_p - t$ and corresponding values of $r_{\min}$ (see inset) range over 3 and 2 decades, respectively. The figure shows

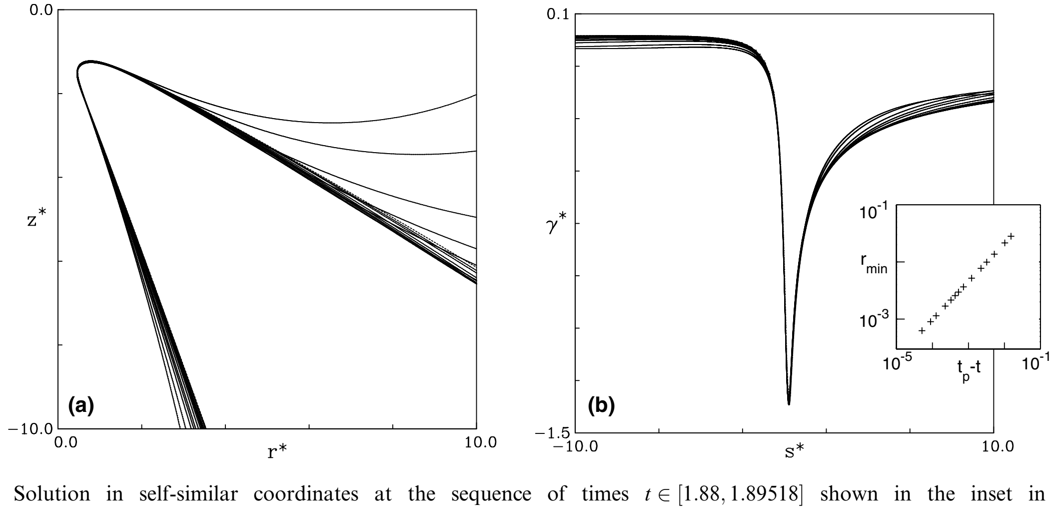

Fig. 10. Solution in self-similar coordinates at the sequence of times $t \in [1.88, 1.89518]$ shown in the inset in (b), for $A = 0, N = 4000, \epsilon_{\max} = 0.99$. (a) (r^*, z^*), (b) (γ^*, s^*).

a large portion of the cone–crater structure collapsing onto one curve as $t_p - t \rightarrow 0$. One characteristic of this structure is $(r^*_{\min}, z^*_{\min})$, the point of minimum radius. Here,

$$(r^*_{\min}, z^*_{\min}) = (0.453, -1.53). \tag{4.3}$$

As will be seen later, these values are in good agreement with the ones obtained by LL for different initial conditions, giving evidence that the structure is independent of the far-field flow. Fig. 10(b) plots the vortex sheet strength vs. arclength in self-similar coordinates

$$\gamma^* = \gamma(t_p - t)^{1/3}, \quad s^* = \frac{s - s_0}{(t_p - t)^{2/3}}, \tag{4.4}$$

at the same sequence of times indicated in the inset, where s_0 is the arclength parameter at the upper point of minimal radius. The sheet strength collapses onto one curve with minimum value

$$\gamma^*_{\min} = -1.38. \tag{4.5}$$

The apparent self-similar structure (r^*, z^*) in Fig. 10(a) has often been characterized as having well-defined angles on each of the cone and crater branches (see, for example, LL). The underlying assumption is that as $t \rightarrow t_p$, the angles on each branch approach a constant as $s^* \rightarrow \pm\infty$. Another criterion used to characterize the structure is whether the inflection point on each branch, that is, the point where the curvature κ_z changes sign, is contained in the self-similar regime or not. If so, then the angle θ attains a local extremum at some finite value of the self-similar coordinate s^*, in the limit as $t \rightarrow t_p$. If not, the extremum is attained at a finite value of the arclength s in the limit as $t \rightarrow t_p$.

In order to investigate the extent to which the current results meet these criteria, Fig. 11 plots the self-similar variables θ vs. s^* at a sequence of times approaching t_p, following [8]. As time increases towards t_p, the curves move in direction of the arrows shown. Fig. 11(a) plots the data at a large scale, for $-10 \leqslant s^* \leqslant 10$. These values of s^* correspond approximately to the values of r^*, z^* plotted in Fig. 10(a). The point of minimal radius corresponds to $\theta = 90°, s^* = 0$. The cone-side corresponds to $s^* < 0$, the crater-side corresponds to $s^* > 0$. At the scale shown in Fig. 11(a), it appears that the curves collapse on both sides as $t \rightarrow t_p$, onto one curve that approaches a constant both as $s^* \rightarrow \infty$ (crater side) and as $s^* \rightarrow -\infty$ (cone side). However, the closeups in Figs. 11(b) and (c) show a marked difference between the cone- and the crater-sides. On the cone-side (Fig. 11(b)), the curves indeed appear to collapse to a limiting curve that approaches a constant angle as $s^* \rightarrow -\infty$ of approximately 110°, in close agreement with the value 109.9° reported by LL. Furthermore, the limiting curve in Fig. 11(b) contains a local maximum at a finite value of s^*,

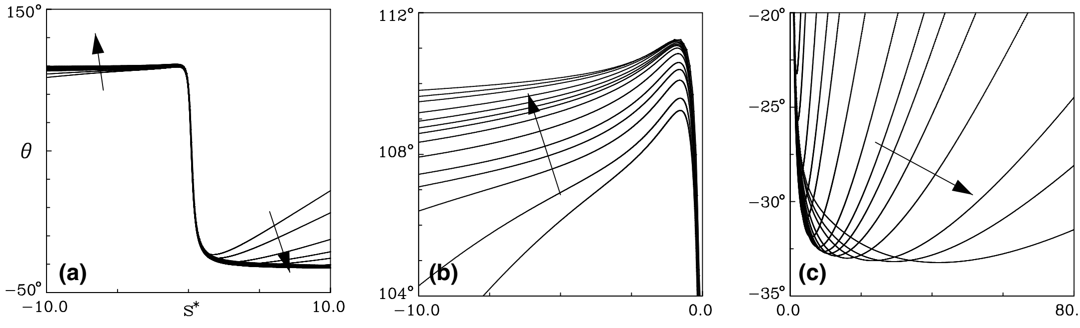

Fig. 11. Angle θ vs. self-similar arclength s^*, at a sequence of times $t \in [1.88, 1.89518]$, for $A = 0, N = 4000, \epsilon_{\max} = 0.99$. Time increases in direction of the arrows shown. Figs. (a–c) plot the same data at different scales.

corresponding to the inflection point on the cone-side. Thus, the self-similar regime on the cone-side contains the inflection point and approaches a constant angle as $s^* \to -\infty$.

The curves on the crater-side (Fig. 11(c)) also contain a local extremum (local minimum) at the corresponding inflection point. However, these curves do not appear to collapse except possibly over a small portion of the interval shown. In particular, the position of the inflection point, in self-similar coordinates s^*, does not converge as $t \to t_{\mathrm{p}}$, and the angle θ does not appear to approach a constant as $t \to t_{\mathrm{p}}$, $s^* \to \infty$. The self-similar regime on the crater-side therefore does not contain the inflection point, and does not appear to have a well-defined angle associated with it. From Fig. 11(c) it is actually not clear what the extent of the self-similar regime on the crater-side is, if any.

One may argue that the times plotted in Fig. 11(c) are not sufficiently close to t_{p} to observe convergence, or that the results are not sufficiently resolved. To address this concern and further support the claim on the difference between the two branches, Fig. 12 plots the position of the inflection points on the cone-side (solid curves) and the crater-side (dashed curves). The position is defined by the corresponding values of $s = s_{\mathrm{I}}$ and $s^* = s^*_{\mathrm{I}}$. Fig. 12(a) shows that as $t_{\mathrm{p}} - t \to 0$, the self-similar variable s^*_{I} converges to a finite value on the cone-side, but diverges on the crater-side. In agreement, the distance $s_{\mathrm{I}} - s_0$ shown in Fig. 12(b) converges to zero on the cone-side, but converges to a nonzero value on the crater-side. Both of these plots give evidence that the inflection point on the crater-side is not in the self-similar regime, in contrast to the one on the cone-side. The results in Fig. 12 are plotted for various values of $N, \epsilon_{\max}$ (see caption). The fact that they remain unchanged as $N, \epsilon_{\max}$ varies gives evidence that they are resolved, and that the conclusions hold under mesh refinement.

We note that the reasons for the documented differences between the cone- and the crater-side are not yet fully understood and remain to be investigated.

4.3. Evolution for $A \neq 0$

Fig. 13 plots the solutions for a range of Atwood numbers $A \in [-0.6, 0.7]$, at a time near pinchoff. For $A \neq 0$, they were computed using $N = 2000$, $\epsilon_{\max} = 0.995$. These cases are more time-consuming to compute than the case $A = 0$, in view of the Fredholm integral equation for γ_t that needs to be solved iteratively at

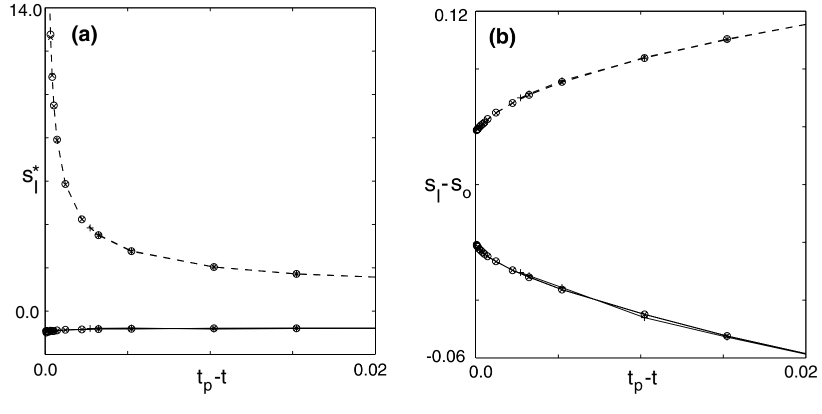

Fig. 12. Position of the inflection points on the cone branch (solid curves) and on the crater branch (dashed curves), for $A = 0$ and $N, = 4000, 0.99$ (○), $N, = 2000, 0.99$ (×), $N, \epsilon_{\max} = 4000, 0.0$ (+). (a) Self-similar coordinate s^*_{I}, (b) arclength coordinate $s_{\mathrm{I}} - s_0$, where s_0 is the arclength at the point of minimal radius.

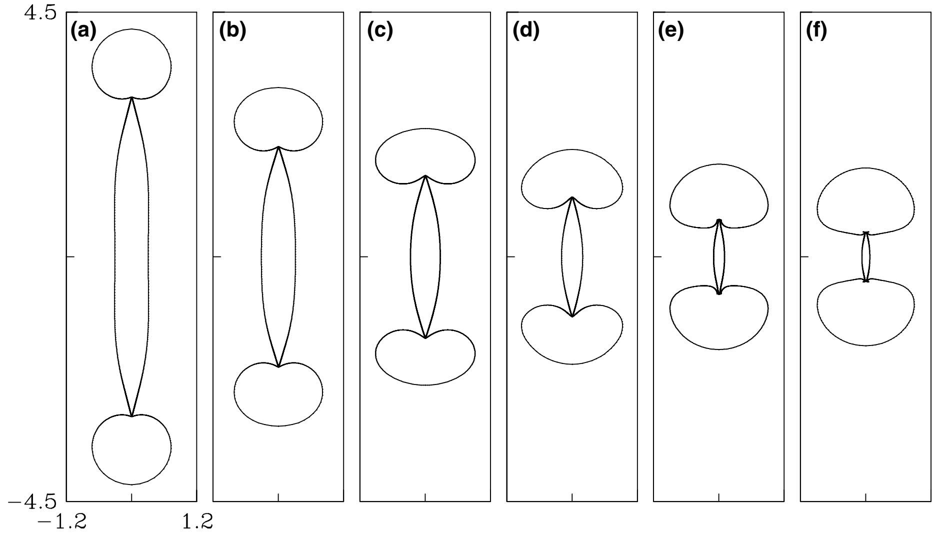

Fig. 13. Solution at a time near pinchoff for a range of values of A. (a) $A = -0.6$, $t = 3.7882$. (b) $A = -0.3$, $t = 2.6198$. (c) $A = 0.0$, $t = 1.89518$. (d) $A = 0.3$, $t = 1.3872$. (e) $A = 0.6$, $t = 1.0005$. (f) $A = 0.7$, $t = 0.8980$. All runs with $A \neq 0$ are computed using $N = 2000, \epsilon_{\max} = 0.995$.

each timestep. To illustrate, the runs with $N = 2000, A \neq 0$ took about 6 days on a 2.2 GHz PC, whereas the $N = 4000$, $A = 0$ run took 5 days on the same machine.

Fig. 13 shows that the shape of both the satellite and the end-bubbles depends significantly on the Atwood number. For $A = -0.6$ (Fig. 13(a)), the satellite bubble at pinchoff is long and the end-bubbles are far apart. Furthermore, the end-bubbles appear to be almost spherical with small crater depth. As A increases, the satellite bubble at pinchoff becomes shorter and smaller and the end-bubbles are closer to each other. The shape of the end-bubbles becomes more elliptical and the crater depth increases until approximately $A = 0.3$ (Fig. 13(d)). For larger values of A (Figs. 13(e) and (f)), the crater depth appears to decrease again, although the end-bubbles remain nonspherical. For reference, increasing values of A corresponds to increasing outer densities relative to the inner ones.

The local shape near the pinchoff point also depends on A. Fig. 14 plots a closeup of the solution at a sequence of times near pinchoff. While the behaviour on the cone-side does not appear to vary much with A, the angles on the crater-side become notably steeper as A increases. For $A = 0.6$, the angle near the pinchoff point is quite steep and a bulge forms nearby. For $A = 0.7$, this bulge has elongated forming a “tongue” of the heavier outer fluid protruding into the inner fluid. At the last times plotted, a second such tongue appears. Thus, the flow is not in the self-similar regime yet, although it does seem to enter the self-similar regime after the development of the second tongue. By computing these flows with $N = 1000$ and $N = 2000$, it was confirmed that the tongues remain unchanged under mesh refinement and are not an artifact of underresolution.

Structures such as seen here for $A = 0.6$, 0.7 are also seen in the computations presented by LL. From those and the present results, it appears that as A increases, the number of tongues increases and the self-similar regime is reached later, at smaller values of $t_p - t$, after the tongues are established. In practice, the small scale features associated with the tongues would likely lead to sub-satellites through nonaxisymmetric instability, suggesting a means to generate a bimodal size distribution of bubbles (or droplets), something that is difficult to do technologically.

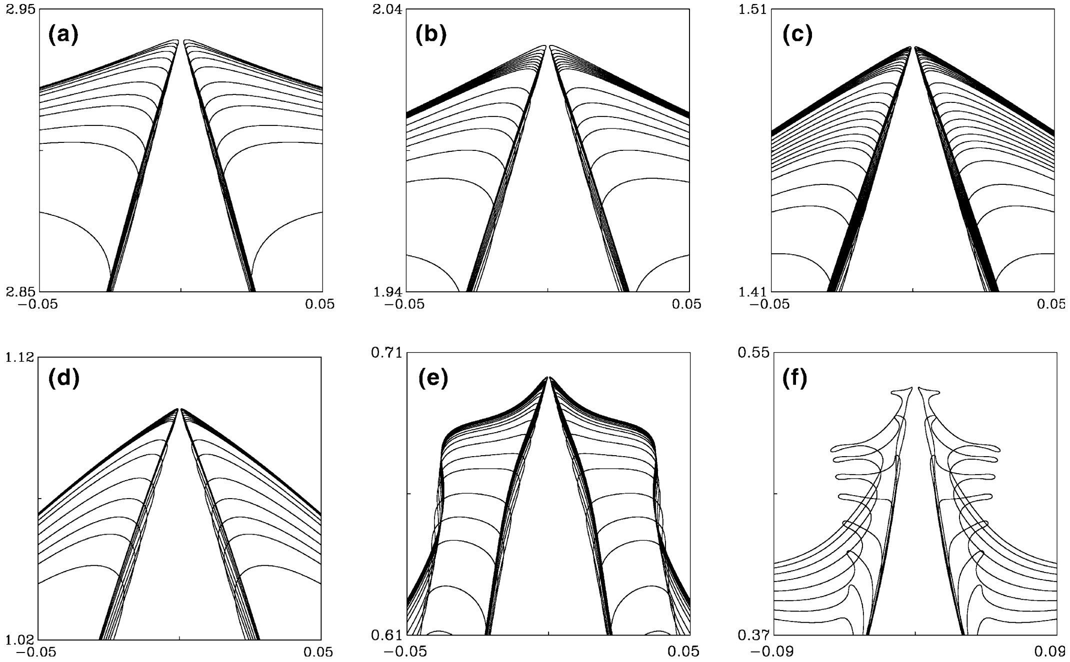

Fig. 14. Closeup of solution for a range of Atwood number $A \in [-0.6, 0.7]$, at the sequence of times indicated in the closeup in Fig. 13: (a) $A = -0.6$, (b) $A = -0.3$, (c) $A = 0.0$, (d) $A = 0.3$, (e) $A = 0.6$ and (f) $A = 0.7$.

4.4. Self-similar collapse, $A \neq 0$

To further document the behaviour near pinchoff, Fig. 15 plots the solution in self-similar coordinates at the sequence of times $t_p - t$ indicated in the insets, for $A \in [-0.6, 0.6]$. For each $A \neq 0$, the pinchoff time t_p is obtained in the same way as for $A = 0$. The values of t_p are close to the times plotted in Fig. 13 and will be recorded in Section 4.5. The case $A = 0.7$ is excluded here since not enough data is available in the self-similar regime.

From the figure, it is apparent that the self-similar regime on the cone-side is reached more slowly for $A = 0.3, 0.6$ than for smaller values of A. In particular, for $A = 0.6$, the smallest values of $t_p - t$ plotted have barely entered the self-similar regime, while those same values of $t_p - t$ are well within the self-similar regime for smaller values of A. This agrees with the earlier statement that self-similarity is reached later, that is, for smaller values of $t_p - t$, as A increases. Furthermore, it is apparent in all plots that the self-similar collapse is approached more slowly on the crater-side (if at all, see earlier remarks) than on the cone-side. Finally, as already seen in Fig. 14, the cone-side depends less on A than the crater-side.

LL computed the self-similar structure obtained in the limit as $t \rightarrow t_p$ by solving local equations near pinchoff in self-similar coordinates, and report the coordinates $(r^*_{\min}, z^*_{\min})$ of the point of smallest radius r^*. Since these values depend on the length scale of the problem, Fig. 16(a) compares the quotient $z^*_{\min}/r^*_{\min}$ (which does not depend on the length scale used) with the results reported in LL. The figure shows good agreement of the present values (diamonds) with those of LL (circles), indicating that the self-similar structure is independent of initial conditions and the far-field flow, as expected. The deviation from LL (less than 0.5%) is attributed to accuracy errors in the present data.

In order to compare the actual values of $r^*_{\min}$, it is necessary to first determine the ratio between the scales in the present results and the ones by LL. Consider the characteristic timescale

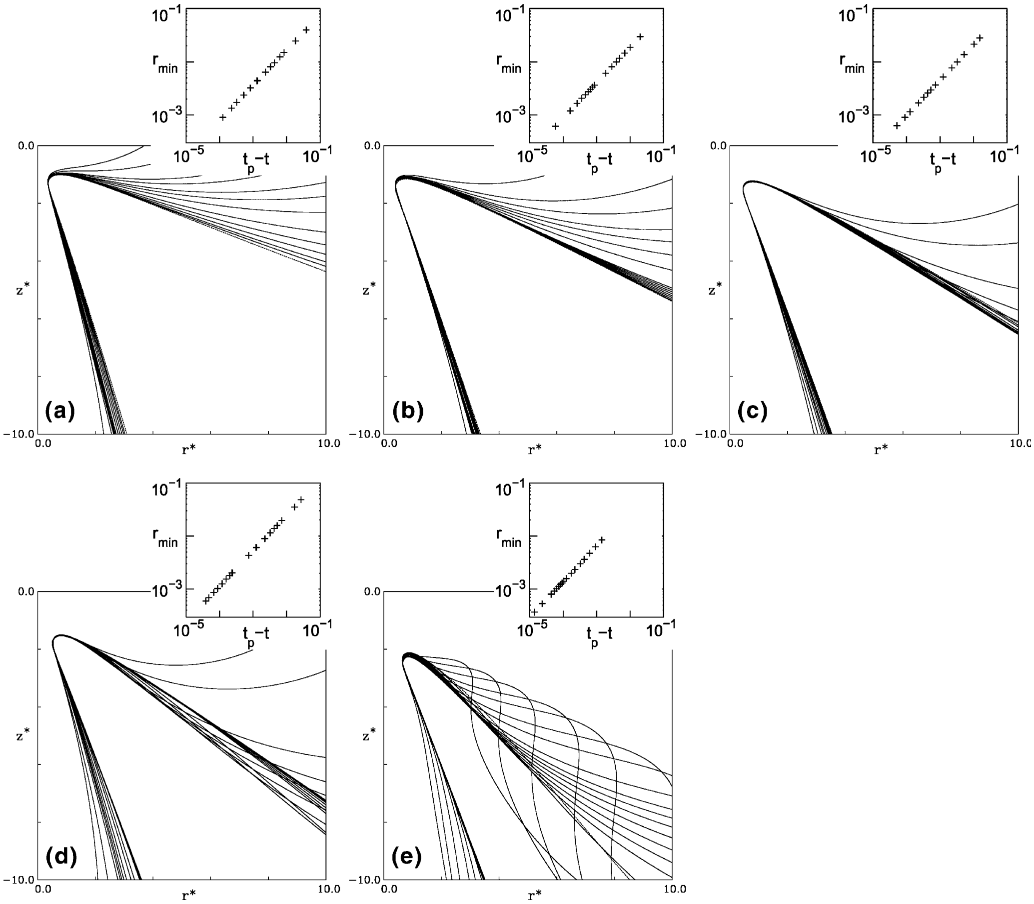

Fig. 15. Solution in self-similar coordinates r^*, z^*, at the times indicated in the inset. (a) $A = -0.6$, (b) $A = -0.3$, (c) $A = 0$, (d) $A = 0.3$ and (e) $A = 0.6$.

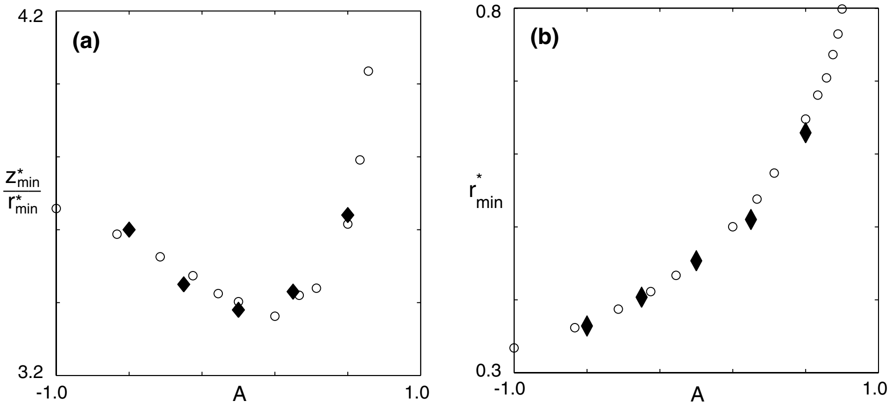

Fig. 16. Position $(r^*_{\min}, z^*_{\min})$ of point of minimal radius in self-similar coordinates. The present results (diamonds) are compared to scaled results by LL (circles). (a) Ratio $z^*_{\min}/r^*_{\min}$, and (b) minimal radius $r^*_{\min,NS}$ and $r^*_{\min,LL}(0.2/(1-A))^{1/3}$.

$$T = \left(\frac{L^3 \rho_{\mathrm{av}}}{\tau} \right)^{1/2}, \tag{4.6}$$

where τ is surface tension and L is a characteristic length scale. From Eq. (4.2), it follows that near pinchoff, r^* scales as $(L/T^{2/3}) = (\rho_{\mathrm{av}}/\tau)^{-1/3}$. As a result the scale ratio should equal

$$\frac{r^*_{\mathrm{NS}}}{r^*_{\mathrm{LL}}} = \left(\frac{\tau_{\mathrm{NS}}}{\rho_{\mathrm{av}}} \frac{\rho_{\mathrm{av}}}{\tau_{\mathrm{LL}}} \right)^{1/3} = \left(\frac{\tau_{\mathrm{NS}}}{\rho_{\mathrm{av}}} \frac{\rho_{\mathrm{av}}}{\rho_1} \frac{\rho_1}{\tau_{\mathrm{LL}}}, \right)^{1/3}, \tag{4.7}$$

where subscripts NS and LL denote the values used in this paper and by LL, respectively. Substituting the identity $\rho_1/\rho_{\mathrm{av}} = 1 - A$ and the values $\tau_{\mathrm{NS}}/\rho_{\mathrm{av}} = 0.2$ and $\tau_{\mathrm{LL}}/\rho_1 = 1$ used in the respective papers, it follows that

$$r^*_{\mathrm{NS}} = r^*_{\mathrm{LL}} \left(\frac{0.2}{1 - A} \right)^{1/3}. \tag{4.8}$$

Fig. 16(b) plots $r^*_{\mathrm{min,NS}}$ (diamonds) and $r^*_{\mathrm{min,LL}}(0.2/(1-A))^{1/3}$ (circles) for a range of values of A, showing that indeed these quantities agree quite well.

4.5. Satellite bubble volume and pinchoff time

An aspect of pinchoff and satellite bubble formation that one wishes to control in engineering applications is the size of the satellite bubble. Fig. 13 shows that it depends significantly on the Atwood number A, or equivalently, on the density ratio across the bubble. Fig. 17(a) plots the satellite bubble volume as a function of A, showing that it decreases sharply as A increases. While the overall enclosed volume is constant (and equal to the initial volume) in all cases, the satellite bubble volume decreases from about 50% to almost 0.5% of the total volume over the range of Atwood numbers shown. As a check on the accuracy of the computations, we confirmed that the total volume for $A = 0.7$ is conserved to within 0.1% throughout the simulation.

The pinchoff time t_p also depends significantly on A. Fig. 17(b) plots t_p as a function of A, and shows that as A increases, or, equivalently, the outer density increases relative to the inner one, the pinchoff time decreases. It decreases by about a factor of 3 over the range of Atwood numbers shown.

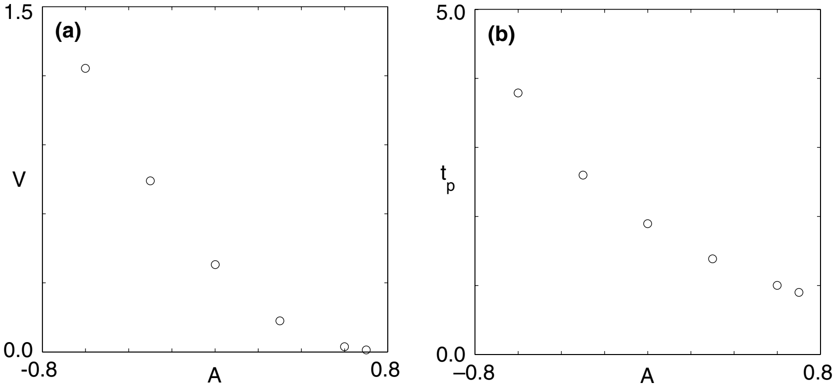

Fig. 17. (a) Satellite bubble volume V, and (b) pinchoff time t_p, as function of Atwood number A.

5. Summary

Inviscid capillary pinchoff of an initially spherical bubble is computed for a range of Atwood numbers $A \in [-0.6, 0.7]$, corresponding to outer/inner density ratios $\rho_2/\rho_1 \in [0.25, 5.7]$. The numerical method is based on a formulation in θ–s_α–$\tilde{\gamma}$ variables and includes a new method to dynamically redistribute the computational meshpoints so that they cluster near the pinchoff point. The method is based on prescribing an evolution equation for s_α. Comparison of solutions with and without local refinement, as well as solutions with increasing number of points, shows that this mesh refinement technique yields convergent results.

The initially spherical vortex sheet pinches in finite time t_p at two points on the symmetry axis, separating the bubble into two symmetric end-bubbles and a satellite bubble. The dynamics near the pinchoff time are resolved to within times $10^{-4} \leqslant t_\mathrm{p} - t \leqslant 10^{-5}$ for all Atwood numbers considered. The conclusions from the simulations can be summarized as:

- The shapes of the asymptotic structure as $t \to t_\mathrm{p}$ appear to be self-similar. Details of the self-similar cone–crater structure, such as the coordinates of the point of minimum radius and the angles on the cone-side, agree with values computed by LL from different initial conditions, using a different numerical method. Furthermore, complex structures that develop near pinchoff for $A \geqslant 0.6$ also agree with results presented by LL.
- The self-similar shape is reached slower, that is, at smaller times $t_\mathrm{p} - t$, for larger values of $A > 0$. It is also reached slower on the crater-side than on the cone-side. On the cone-side, the asymptotic self-similar shape approaches a constant angle as $|s^*| \to \infty$, and includes the inflection point. The crater does not appear to approach a constant angle as $|s^*| \to \infty$ and the self-similar region does not include the inflection point. The extent to which the crater side is self-similar and the reasons for the observed differences between the cone- and crater-side remain to be further investigated.
- On a larger scale, it is found that the satellite bubble volume and the pinchoff time depend significantly on the Atwood number. The satellite bubble volume decreases by a factor of 100 as A increases from -0.6 to 0.7, while the pinchoff time decreases by a factor of 3.

Acknowledgements

We are grateful to John Lister for helpful suggestions that led to the scaling arguments used for Fig. 16 and for supplying us with the raw data. We also thank Robert Krasny and two anonymous referees for many helpful comments that improved the clarity and accuracy of the presentation. M.N. gratefully acknowledges the National Science Foundation for support under Grant DMS-0308061. P.H.S. thanks NASA for support under Grant NAG3-2713.

Appendix A. Behaviour of $\kappa_{r,s}$ near endpoints

The vortex sheet touches the axis at the two points $s = 0$ and $s = L$. Near these points, computing $\kappa_{r,s}$ introduces large roundoff error since it involves division of small numbers. Here, we show that for $s \approx 0$,

$$\kappa_{r,s} = \frac{\kappa_{z,s}}{3} + \mathrm{O}(s^3). \tag{A.1}$$

Since $\kappa_{z,s}$ can be computed accurately near the endpoints, one can reduce the roundoff error in approximating $\kappa_{r,s}$ using (A.1). For simplicity, we denote differentiation with respect to arclength by a prime from here on, $' = \mathrm{d}/\mathrm{d}s$.

First, note that

$$(r', z') = (\cos\theta, \sin\theta), \quad (r'', z'') = (-\sin\theta, \cos\theta)\theta', \tag{A.2a}$$

$$(\kappa_r, \kappa_z) = (z'/r, \theta') = (\sin\theta/r, \theta'), \tag{A.2b}$$

$$(\kappa_r', \kappa_z') = \left(\frac{r'}{r}(\kappa_z - \kappa_r), \theta''\right) = \left(\cos\theta\frac{r\theta' - \sin\theta}{r^2}, \theta''\right). \tag{A.2c}$$

Assume that $r(s), \theta(s)$ are sufficiently smooth at the axis (bounded third derivatives is enough for the present purposes) and use the fact that both functions are odd about $s = 0$ and that $r'(0) = 1$, to obtain Taylor series expansions for κ_r' and κ_z'. To obtain the series for κ_r' first define functions f and g by

$$f(s) = r\theta' - \sin\theta = \frac{s^3}{3}\theta'''(0) + O(s^5), \tag{A.3a}$$

$$g(s) = r^2 = s^2 + O(s^4). \tag{A.3b}$$

Then

$$\kappa_r'(s) = \cos\theta\frac{f(s)}{g(s)} = (1 + O(s^2))\left(\frac{s}{3}\theta'''(0) + O(s^3)\right) = \frac{s}{3}\theta'''(0) + O(s^3). \tag{A.4}$$

The series for κ_z' is given by,

$$\kappa_z'(s) = \theta'' = s\theta'''(0) + O(s^3). \tag{A.5}$$

It follows that

$$\kappa_r'(s) = \kappa_z'(s)/3 + O(s^3). \tag{A.6}$$

Similarly, it holds that for $s \approx L$,

$$\kappa_r'(s) = \kappa_z'(s)/3 + O((L - s)^3). \tag{A.7}$$

References

[1] G.R. Baker, D.I. Meiron, S.A. Orszag, Generalized vortex methods for free surface flow problems, J. Fluid Mech. 123 (1982) 477–501.

[2] G.R. Baker, D.W. Moore, The rise and distortion of a two-dimensional gas bubble in an inviscid liquid, Phys. Fluids A 1 (9) (1989) 1451–1459.

[3] G.R. Baker, A. Nachbin, Stable methods for vortex sheet motion in the presence of surface tension, SIAM J. Sci. Comput. 19 (5) (1998) 1737–1766.

[4] O. Basaran, Small-scale free surface flows with breakup: drop formation and emerging applications, AIChE J. 48 (9) (2002) 1842–1848.

[5] J.T. Beale, T.Y. Hou, J.S. Lowengrub, Growth rates for the linearized motion of fluid interfaces away from equilibrium., Comm. Pure Appl. Math. 46 (9) (1993) 1269–1301.

[6] J.T. Beale, T.Y. Hou, J. Lowengrub, Convergence of a boundary integral method for water waves, SIAM J. Numer. Anal. 33 (5) (1996) 1797–1843.

[7] J.T. Beale, T.Y. Hou, J.S. Lowengrub, M.J. Shelley, Spatial and temporal stability issues for interfacial flows with surface tension, Math. Comput. Modelling 20 (1994) 1–27.

[8] O.N. Boratav, Y.-C. Chen, P.H. Steen, Bubble disconnection: self-similarity and cascading physics, in: J.L. Lumley (Ed.), Fluid Mechanics and the Environment: Dynamical Approaches, Springer, New York, 2001, pp. 19–34.

[9] H.D. Ceniceros, T.Y. Hou, Convergence of a non-stiff boundary integral method for interfacial flows with surface tension, Math. Comput. 67 (221) (1998) 137–182.

[10] H.D. Ceniceros, T.Y. Hou, H. Si, Numerical study of Hele–Shaw flow with suction. Phys, Fluids 11 (9) (1999) 2471–2486.

[11] H.D. Ceniceros, H. Si, Computation of axisymmetric suction flow through porous media in the presence of surface tension, J. Comp. Phys. 165 (1) (2000) 237–260.

[12] A.U. Chen, P.K. Notz, O.A. Basaran, Computational and experimental analysis of pinch-off and scaling, Phys. Rev. Lett. 88 (4) (2002) 174501.

[13] Y.-C. Chen, P.H. Steen, Dynamics of inviscid capillary breakup: collapse and pinchoff of a film bridge, J. Fluid Mech. 341 (1997) 245–267.

[14] B. de Bernadinis, D.W. Moore, A ring-vortex representation of an axi-symmetric vortex sheet, in: M.Y. Hussaini, M.D. Salas (Eds.), Studies of Vortex Dominated Flows, Springer, New York, 1987, pp. 33–43.

[15] R.F. Day, E.J. Hinch, J.R. Lister, Self-similar capillary pinchoff of an inviscid fluid, Phys. Rev. Lett. 80 (4) (1998) 704–707.

[16] J. Eggers, Universal pinching of 3D axisymmetric free-surface flow, Phys. Rev. Lett. 71 (21) (1993) 3458–3460.

[17] J. Eggers, T.F. Dupont, Drop formation in a one-dimensional approximation of the Navier-Stokes equation, J. Fluid Mech. 262 (1994) 205–221.

[18] R. Goldstein, D.M. Petrich, The Korteweg–de Vries hierarchy as dynamics of closed curves in the plane, Phys. Rev. Let. 67 (1991) 3203–3206.

[19] T. Hou, J. Lowengrub, M. Shelley, Removing the stiffness from interfacial flows with surface tension, J. Comp. Phys. 114 (1994) 312–338.

[20] T. Hou, J. Lowengrub, M. Shelley, The long time motion of vortex sheets with surface tension, Phys. Fluids 9 (7) (1997) 1933–1954.

[21] T.Y. Hou, J.S. Lowengrub, M.J. Shelley, Boundary integral methods for multicomponent fluids and multiphase materials, J. Comp. Phys. 169 (2001) 302–362.

[22] D.A. Kessler, J. Koplik, H. Levine, Geometrical models of interface evolution, II Phys. Rev. A 30 (1984) 3161–3174.

[23] J.B. Keller, Breaking of liquid films and threads, Phys. Fluids. 26 (12) (1983) 3451–3453.

[24] J.B. Keller, M. Miksis, Surface tension driven flows, SIAM J. Appl. Math. 43 (2) (1983) 268–277.

[25] J.B. Keller, A. King, L. Ting, Blob formation, Phys. Fluids 7 (1) (1995) 226–228.

[26] R. Krasny, A study of singularity formation in a vortex sheet by the point-vortex approximation, J. Fluid Mech. 167 (1986) 65–93.

[27] D.M. Leppinen, J.R. Lister, Capillary pinch-off in inviscid fluids, Phys. Fluids 15 (2003) 568–578.

[28] N. Mansour, T.S. Lundgren, Satellite formation in capillary jet breakup, Phys. Fluids A. 2 (7) (1990) 1141–1144.

[29] E. Meiburg, G.M. Homsy, Nonlinear unstable viscous fingers in Hele–Shaw flows. 2. Numberical simulation, Phys. Fluids 31 (3) (1988) 429–439.

[30] Q. Nie, The nonlinear evolution of vortex sheets with surface tension in axisymmetric flows, J. Comp. Phys. 174 (2001) 438–459.

[31] Q. Nie, G. Baker, Application of adaptive quadrature to axi-symmetric vortex sheet motion, J. Comp. Phys. 143 (1998) 49–69.

[32] M. Nitsche, Axisymmetric vortex sheet motion: accurate evaluation of the principal value integral, SIAM J. Sci. Comput. 21 (3) (1999) 1066–1084.

[33] M. Nitsche, Singularity formation in a cylindrical and a spherical vortex sheet, J. Comp. Phys. 173 (2001) 208–230.

[34] D.T. Papageorgiou, Analytical description of the breakup of liquid jets, J. Fluid. Mech. 301 (1995) 109–132.

[35] D.T. Papageorgiou, O. Orellana, Study of cylindrical jet breakup using one-dimensional approximations of the Euler equations, SIAM J. Appl. Math. 59 (1) (1998) 286–317.

[36] D.H. Peregrine, G. Shoker, A. Symon, The bifurcation of liquid bridges, J. Fluid Mech. 212 (1990) 25–39.

[37] D.I. Pullin, Numerical studies of surface tension effects in nonlinear Kelvin–Helmholtz and Rayleigh–Taylor instability, J. Fluid Mech. 119 (1982) 507–532.

[38] R.H. Rangel, W.A. Sirignano, Nonlinear growth of Kelvin–Helmhotz instability: effect of surface tension and density ratio, Phys. Fluids 31 (7) (1988) 1845–1855.

[39] N.D. Robinson, P.H. Steen, Observations of singularity formation during the capillary collapse and bubble pinch-off of a soap film bridge, J. Colloid and Interface Science 241 (2001) 448–458.

[40] Y. Saad, M. Schultz, GMRES: A generalized minimal residual algorithm for solving nonsymmetric linear systems, SIAM J. Sci. Statist Comput. 7 (1986) 856–869.

[41] X.D. Shi, M.P. Brenner, S.R. Nagel, A cascade of structure in a drop falling from a faucet, Science 265 (1994) 219–222.

[42] M.J. Shelley, M. Vinson, Coherent structures on a boundary layer in Rayleigh–Bénard turbulence, Nonlinearity 5 (1992) 323–351.

[43] R.M.S.M. Schulkes, The contraction of liquid filaments, J. Fluid Mech. 309 (1996) 277–300.
[44] P.H. Steen, Y.-J. Chen, Contacting and forming singularites: distinguishing examples, Chaos 9 (1) (1999) 164–172.
[45] J. Strain, A boundary integral approach to unstable solidification, J. Comp. Phys. 85 (1989) 342–389.
[46] L. Ting, J.B. Keller, Slender jets and thin sheets with surface tension, SIAM J. Appl. Math. 50 (6) (1990) 1533–1546.